Fabrication of Highly Uniform Nanoparticles from Recombinant Silk-Elastin-like Protein Polymers for Therapeutic Agent Delivery

Rajasekhar Anumolu,[†] Joshua A. Gustafson,[‡,§] Jules J. Magda,[†,⊥] Joseph Cappello,[∥] Hamidreza Ghandehari,[‡,§,∥] and Leonard F. Pease III[†,§,∥,#,*]

[†]Department of Chemical Engineering, University of Utah, Salt Lake City, Utah 84112, United States, [‡]Department of Bioengineering, University of Utah, Salt Lake City, Utah 84112, United States, [§]Utah Center for Nanomedicine, Nano Institute of Utah, University of Utah, Salt Lake City, Utah 84108, United States, [⊥]Department of Materials Science & Engineering, University of Utah, Salt Lake City, Utah 84112, United States, [∥]Department of Pharmaceutics & Pharmaceutical Chemistry, University of Utah, Salt Lake City, Utah 84112, United States, and [#]Department of Internal Medicine, University of Utah, Salt Lake City, Utah 84132, United States

ABSTRACT Here we generate silk-elastin-like protein (SELP) polymeric nanoparticles and demonstrate precise control over their dimensions using an electrospray differential mobility analyzer (ES-DMA). Electrospray produces droplets encompassing several polymer strands. Evaporation ensues, leading polymer strands to accumulate at the droplet interface, forming a hollow nanoparticle. The resulting nanoparticle size distributions, which govern particle yield, depend on buffer concentration to the −1/3 power, polymer concentration to the 1/3 power, and ratio of silk-to-elastin blocks. Three recombinantly tuned ratios of 8:16, 4:8, and 4:16, respectively named SELP-815K, SELP-47K, and SELP-415K, are employed, with the latter ratio resulting in a thinner shell and larger diameter for the nanoparticles than the former. The DMA narrows the size distribution by electrostatically classifying the aerosolized nanoparticles. These highly uniform nanoparticles have variations of 1.2 and 1.4 nm for 24.0 and 36.0 nm particles, respectively. Transmission electron microscopy reveals the nanoparticles to be faceted, as a buckling instability releases compression energy arising from evaporation after the shell has formed by bending it. A thermodynamic equilibrium exists between compression and bending energies, where the facet length is half the particle diameter, in agreement with experiments. Rod-like particles also formed from polymer-stabilized filaments when the viscous length exceeds the jet radius at higher solution viscosities. The unusual uniformity in composition and dimension indicates the potential of these nanoparticles to deliver bioactive and imaging agents.

KEYWORDS: recombinant polymers · silk-elastin-like protein polymers · nanoparticles · hydrogels · jet-breakup · drug delivery · gas-phase electrophoretic mobility molecular analysis

Nanoparticles are widely used for a variety of biomedical applications including targeted drug and gene delivery. Particles for these purposes include elastin-like protein and poly(L-lysine) and poly(L-glutamic acid) fabricated using a layer-by-layer technique are often hollow and several micrometers in diameter.[1,2] However, most nanoparticles with refined size[3,4] (*i.e.*, where the ratio of standard deviation in the diameter to the mean diameter is ∼0.06−0.13) are composed of metallic particles with potential toxicity issues (quantum dots, silver particles, *etc.*). In this work we examine a new way to fabricate highly uniform nanoparticles from recombinant silk-elastin-like protein polymers (SELPs), an important class of genetically engineered biomaterials, recently used for localized gene delivery applications.[5] Combining precise control over nanoparticle size with precise control over polymer structure enabled by recombinant techniques presents a unique opportunity to precisely tune the payload and rate of release of the therapeutic agents as well as their biological fate.

SELPs were first developed by Cappello and co-workers[6] and are composed of amino acid sequence motifs from two naturally occurring proteins: *Bombyx mori* (silkworm) silk (Gly-Ala-Gly-Ala-Gly-Ser) and mammalian elastin (Gly-Val-Gly-Val-Pro). By combining the silk-like and elastin-like blocks in several ratios and sequences, it is possible to produce an array of SELPs with diverse material properties useful for controlled delivery.[7] In contrast to traditional polymers used as matrixes for gene and drug delivery that are heterogeneous in composition, length, or both, it has been shown that solubility, gelation, material strength, stimuli-sensitivity, biodegradation, and drug and gene release profiles of SELPs can be precisely controlled by varying the composition and sequence of the polymers.[8−20] Compared to elastin-based polymers, the silk units in SELPs enable robust hydrogel formation without the need to introduce cross-linking agents. SELPs are biocompatible

* Address correspondence to pease@eng.utah.edu.

Received for review December 23, 2010 and accepted June 22, 2011.

Published online June 22, 2011
10.1021/nn103585f

when used as implants and do not contain toxic monomer residues and solvents. SELP copolymers, depending on the number and sequence of silk and elastin blocks, undergo an irreversible sol-to-gel transition,[8,16] which is accelerated at body temperature. This accelerated gelation enhances the utility of these copolymers for local treatment modalities, since they can be locally injected in liquid form, gel at body temperature, and gradually release bioactive agents with time scales set by the structure and concentration of the polymer.[19]

Despite significant advances made with these polymers for localized gene delivery,[5] they have primarily been used for direct injection into tissues such as solid tumors, which due to poor accessibility and patient inconvenience limits the broader application of these polymers. Developing SELPs into nanoparticles that can systemically administer bioactive agents to target sites would be advantageous. Several techniques are available to fabricate polymeric nanoparticles including electrohydrodynamic atomization, microfluidic flow focusing devices, and flash nanoprecipitation.[21−29] However, these methods are expensive and time-consuming and fail to produce particles over smaller size ranges (*i.e.*, $\leq$ 100 nm) or fail to do so precisely. Electrospray has also been used to produce nanoparticles from elastin-like polypeptide and poly(L-lactic acid).[30,31] However, these nanoparticles have higher coefficients of variation (32−40%) relative to those reported here (5%), as explained later. Template techniques were also used to produce a monodispersed population of elastin-like hollow spheres.[32,33] Here, in contrast we examine the potential for electrospray-differential mobility analysis (ES-DMA) to both directly *generate* and *purify* polymeric nanoparticles without the addition of hazardous solvents (see Figure 1a). ES-DMA can detect particles from 3 to 700 nm and can do so with subnanometer precision.[34]

Here we propose to extend the advantages of SELP matrixes to systemic drug and gene delivery by forming them into nanoparticles using ES-DMA. Three distinct SELP structures, SELP-47K, SELP-415K, and SELP-815K, which are named after their number of silk and elastin repeats (see Table 1), were synthesized previously and evaluated for therapeutic purposes for matrix-mediated drug and gene delivery.[18,19,35] Each block has one elastin unit containing a lysine residue, designated by K. In this article, we form these SELPs into nanoparticles, investigate their yield, demonstrate that they can be purified with remarkable uniformity of size, explore the parameters that govern particle structure, and show that these nanoparticles can encapsulate model therapeutic agents.

RESULTS AND DISCUSSION

The primary hypothesis of this article is that SELP nanoparticles can be produced with controlled yield and selectivity. These highly uniform nanoparticles form from electrospray droplets that capture multiple polymer strands (see Figure 1a). Evaporation ensues, simultaneously shrinking the droplet diameter and leading to accumulation of polymer at the droplet interface. The polymer forms a thin film or shell around the exterior of the droplet. Further evaporation compresses the shell and concentrates the polymer remaining in the core.

Figure 1b shows a gallery of representative transmission electron microscopy (TEM) images of the nanoparticles thus formed (see Figures S1 and S2 in the Supporting Information for enlarged image and additional nanoparticle images). Most of the nanoparticles are approximately spherical and display modest faceting,

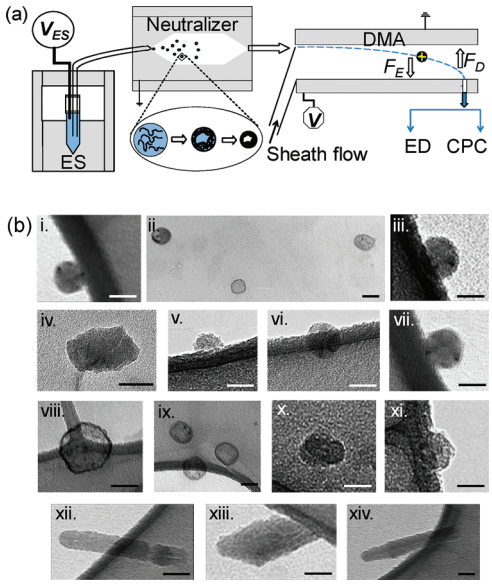

Figure 1. (a) Schematic of electrospray differential mobility analysis (ES-DMA) including electrospray (ES) to generate highly charged droplets enclosing multiple polymer strands; a neutralizer to set the charge on the drying nanoparticles to +1, −1, or 0; a differential mobility analyzer (DMA) to separate particles by their charge-to-size ratio determined trajectory by balancing electrostatic, F_E, and drag forces, F_D; and a condensation particle counter (CPC) to enumerate them or an electrostatic deposition chamber (ED) to deposit them on desired substrates. The magnified droplet depicts the nanoparticle formation process in which the individual polymer strands entangle as the droplet evaporates. (b) Gallery of TEM images of representative SELP nanoparticles. Images i, iii, iv−vii, and xii are composed of SELP-815K. Images ii, viii, and ix are composed of SELP-415K, and the rest are composed of SELP-47K. Scale bar = 25 nm.

TABLE 1. Composition of Silk-Elastin-like Protein Polymers

polymer[a]	silk units	elastin units	silk-elastin blocks/strand	mol. wt (kDa)
SELP-47K	4	8	13	69.8
SELP-415K	4	16	8	71.5
SELP-815K	8	16	6	65.3

[a] Please see Scheme S1 in Supporting Information for amino acid sequences of the polymers.

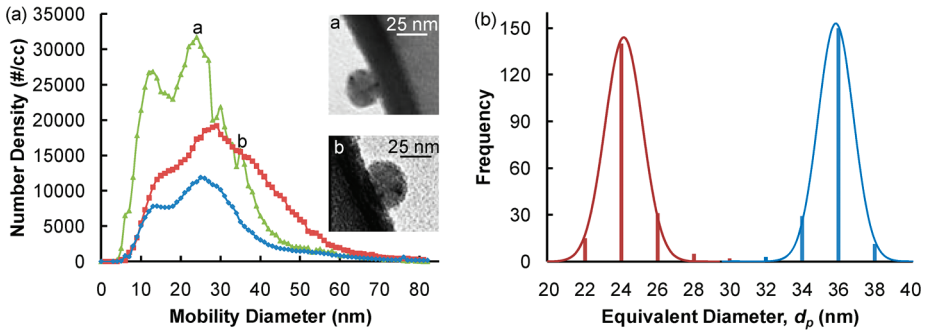

Figure 2. (a) Size distributions of nanoparticles fabricated from polymers SELP-815K (green ▲), SELP-415K (red ■), and SELP-47K (blue ◆) at polymer weight fraction and buffer concentration of w_p = 0.00133 and C_b = 2 mM, respectively. Number density is the number of particles/cm^3 of gas flow through the CPC at a rate of 1.5 L/min. The insets show micrographs of SELP-815K nanoparticles electrostatically collected on TEM grids (dark line) from peaks in the size distribution at 24.0 and 36.0 nm, respectively, to demonstrate the size selectivity of the DMA. (b) Histograms representing the diameter of nominally 24.0 and 36.0 nm SELP-815K nanoparticles as determined from TEM following electrostatic deposition. The mean and standard deviation of the size distribution of these particles are 24.2 ± 1.2 nm and 35.8 ± 1.4 nm, respectively.

although some are elongated with sharp facets. Figure 2 shows that these nanoparticles are also heterogeneous in size, with diameters ranging from 5 nm to over 60 nm, which is not atypical of nanoparticles formed from traditional techniques (see Figure S3a in the Supporting Information). For this reason we purify these nanoparticles by size using a DMA (see Figure 1a). The remainder of this article is dedicated to elucidating the factors that govern the size selectivity, yield, and structure of these SELP nanoparticles.

The prominent feature of these recombinant nanoparticles is their uniformity after size purification through the DMA. Figure 2a shows that prior to separation the particles are heterogeneous in size. The width and mean of the distribution of diameters depend on several factors including the polymer composition. The three SELPs selected for this study have approximately equal molecular weights ranging from 65 to 72 kDa (see Table 1) but distinct silk-to-elastin ratios of approximately 1/2 for SELP-47K and SELP-815K and 1/4 for SELP-415K. Figure 2a suggests that decreasing this ratio leads to wider distributions. However, following size separation using the DMA, the distributions narrow dramatically. The insets to Figure 2a show nanoparticles collected at two sizes, while Figure 2b shows two histograms of the nanoparticle diameter each assembled from nearly 200 TEM images of nominally 24.0 or 36.0 nm SELP particles collected at the indicated positions in Figure 2a.

Statistical compilation and Gaussian curves in Figure 2b show the standard deviation on the diameter of these DMA selected particles to be 1.2 and 1.4 nm for the nominally 24.0 and 36.0 nm sizes, respectively. A Gaussian distribution is not unexpected because Stolzenberg indicates that diffusional broadening within the DMA contributes to instrument uncertainty and follows this distribution.[36,37] In net, this leads to coefficients of variation of ≤5%, which is equal to or better than those reported for metallic nanoparticles and rivals that of biologically assembled particles such as viruses.[3,38−40] These results demonstrate that ES-DMA can both generate and purify polymeric nanoparticles with high dimensional uniformity.

The size distributions also depend on the polymer concentration or weight fraction, w_p, and buffer concentration, C_b (see Figure S3c and S3d in the Supporting Information). These two parameters are important because they provide the ability to tune the yield of particles selected by the DMA by positioning the peak maximum at the diameter selected for size purification. By tuning the experimental conditions (simply changing w_p and C_b), we can optimize the yield (*e.g.*, by lowering C_b and/or raising w_p) to obtain larger particles. Figure 3a shows that increasing w_p leads to larger nanoparticles with a power law dependence of $d_p \sim w_p^{1/3}$. Conversely, Figure 3b shows that increasing C_b leads to smaller nanoparticles with a power law dependence of $d_p \sim C_b^{-1/3}$.

The exponents in Figure 3 follow directly by comparing the polymer mass contained in the droplet before evaporation ($w_p\rho_w\pi d_{drop}^3/6$) and the nanoparticle after evaporation ($\rho_p\pi d_p^3/6$). Equating the two masses gives an expression for the particle diameter, $d_p = (\rho_w/\rho_p)^{1/3} d_{drop} w_p^{1/3}$, where ρ_w and ρ_p are densities of polymer in the droplet and particle, respectively, and d_{drop} is the diameter of the electrospray droplet. Because polymer concentration in the droplet is initially very modest, the density of the droplet is essentially that of pure water. The mass balance immediately explains the dependence of the particle diameter on the weight fraction of the polymer in Figure 3a. Furthermore, de la Mora, *et al.*,[41] reports that d_{drop} depends on the buffer conductivity, κ, as $d_{drop} \sim \kappa^{-1/3}$, and we find experimentally that κ depends linearly on C_b (see Figure S3b in the Supporting Information). Substituting C_b for κ yields $d_p \sim C_b^{-1/3}$, in excellent agreement with Figure 3b.

Figure 3a also illustrates that SELP-415K nanoparticles follow trends distinct from those of SELP-47K

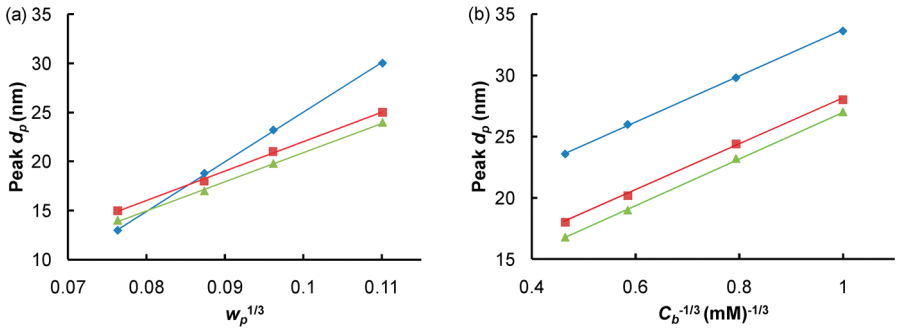

Figure 3. (a) Experimental mobility diameter, d_p (see Figure 2a), *versus* polymer concentration, w_p, to the 1/3 power for SELP-415K (blue ◆), SELP-47K (red ■), and SELP-815K (green ▲) at C_b = 2 mM. (b) Mobility diameter *versus* buffer concentration, C_b, to the −1/3 power at w_p = 0.00133. Linearity confirms choice of exponent.

and -815K, depending on the polymer concentration. As the droplet evaporates, polymer strands accumulate at the interface, forming a shell. When the cross-linking reaction is slower than the evaporation rate, silk and elastin units in the SELPs start to cross-link after the shell has formed. After complete evaporation, compression forces are released, resulting in expansion of the elastin units. The percentages of cross-linkable units in SELP-47K and -815K are similar to one another and approximately double that of 415K.[18] This lower cross-linking density of SELP-415K allows the elastin units to expand more, yielding a particle with larger diameter and thinner shell. However, particles of SELP-47K and -815K remain smaller due to more cross-linking. This prediction of thinner shells in SELP-415K is supported by the shell thickness measurements, which show that SELP-415K, -47K, and -815K have an average shell thickness of 4.8 ± 1.4, 6.0 ± 0.8, and 6.2 ± 0.8 nm, respectively (sample size = 32 shells), for particle sizes of 29, 25, and 24 nm. The difference in the average shell thicknesses of SELP-47K and -415K is significant at a 99% confidence level based on Student's *t* test, whereas that of SELP-47K and -815K is not significant. These observations are also consistent with the physicochemical properties of these polymers investigated previously, where the modulus of elasticity of SELP-415K is lower than that of SELP-47K and SELP-815K.[18]

Surprisingly, several of the SELP particles in Figure 1b are faceted or display nearly straight edges, as magnified in Figure 4a. TEM diffraction studies (data not shown) found no indication of ordering, suggesting that crystallization of the polymer was not responsible for the faceting. However, most of the TEM images suggest an increased density of the polymer on the SELP particle perimeter, and these edges are not sharp as expected of crystallization, leading to the hypothesis that a buckling instability[42] may be responsible for the apparent faceting. In this scenario, electrospray droplets, consisting of SELP, water, and ammonium acetate selected for its volatility, immediately begin to dry. As the solvent evaporates, the polymer strands accumulate at the air−water surface and tangle or gel into a thin film or shell.[43,44] Further evaporation compresses the shell, developing compression stresses that the entangled strands cannot completely relax by shrinking the particle perimeter. As more solvent evaporates through the shell, its compression energy increases further until it becomes energetically favorable for the shell to bend to relieve circumferentially applied compression energy. Figure 4b shows a diagram of this process. Landau and Liftshitz show that the compression and bending energies, E_c and E_b, scale as

$$E_c = \frac{2Eh\delta^2}{{d_p}^2} L_f d_b \text{ and } E_b = \frac{Eh^3\delta^2 L_f}{2{d_b}^3} \quad (1)$$

where E is elastic modulus, h is shell thickness, δ is the displacement of points on the shell from an ideal sphere in the bending strip defined as θd_b (see Figure 4b), and L_f represents the facet length of a SELP nanoparticle (see Figure 4a).[45] In the neighborhood of a bend, the local bending diameter representing the local curvature of the particle is given as d_b, and the diameter of the particle is estimated by summing the lengths of each facet and dividing by π, such that $d_p = \sum_i L_f^i/\pi$. The sum of these two energies may be minimized with respect to d_b to find $d_b = 3^{-1/4}h^{1/2}{d_p}^{1/2}2^{-1/2}$. We scale d_b on L_f such that this dimensionless ratio varies between zero and unity and substitute $L_f = d_p \sin\theta$, where θ is related to the number of sides or facets, n, by $\theta = \pi/n$. Then,

$$\frac{d_b}{L_f} = \frac{3^{-1/4}}{2}\left(\frac{2h}{d_p}\right)^{1/2}\frac{1}{\sin(\pi/n)} \quad (2)$$

Figure 4c shows the relationship between these dimensionless ratios (d_b/L_f and $2h/d_p$) for n ranging from 4 to 8. Each parameter in eq 2 can be estimated experimentally from TEM images (like Figure 4a) for SELP nanoparticles. Comparing experiment to theory in Figure 4c shows good quantitative agreement, confirming the hypothesis that a buckling instability governs facet formation. Remarkably, Figure 4c also indicates that the nanoparticles are essentially hollow with the shell comprising 10−40% of the particle radius. This can be confirmed by a mass balance where the nanoparticle volume is given by $\rho_p\pi[{d_p}^3 - (d_p - h)^3]/6$ such that

$$h = \frac{d_p}{2}\left[1 - w_p\frac{\rho_w}{\rho_p}\frac{{d_{drop}}^3}{{d_p}^3}\right] \quad (3)$$

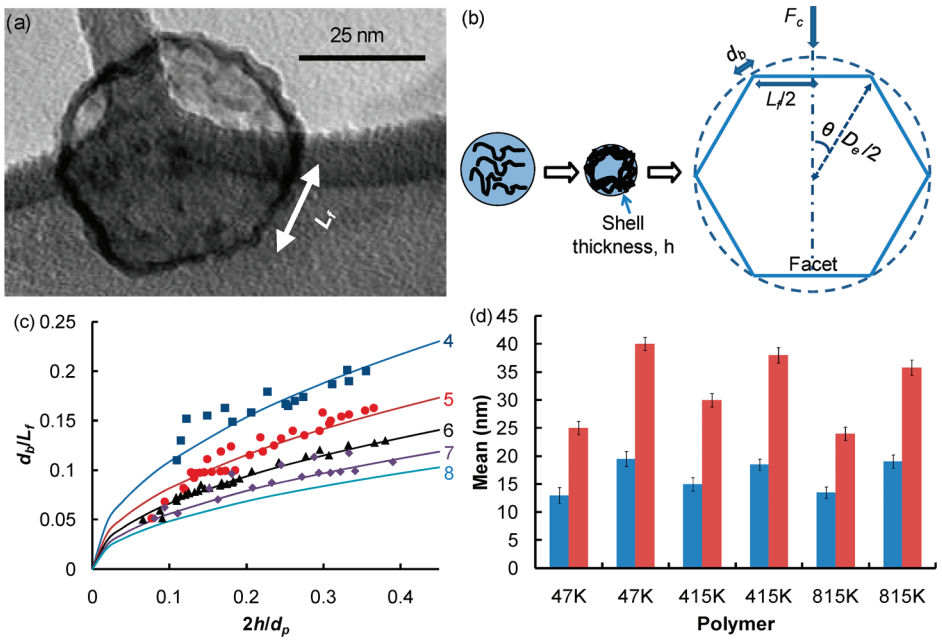

Figure 4. (a) TEM micrograph depicting the length of a facet, L_f, on a 36 nm diameter SELP nanoparticle with $d_b \approx 3-4$ nm. (b) Diagram showing the three stages of SELP nanoparticle growth, namely, (i) evaporation of an electrospray droplet containing polymer strands, (ii) accumulation and entanglement of the strands at the droplet surface until a thin film gels to form a shell of thickness h, and (iii) buckling of the shell to relieve compression energy, F_c, by bending to reveal the facets of panel (a). (c) Ratio of the bend diameter, d_b, to the length of the facet, L_f, *versus* the ratio of the shell thickness, h, to the particle diameter, d_p. The solid lines represent eq 2, the symbols represent color-coordinated experimental data, and the numbers to the right represent the number of facets. (d) The mean and standard deviation (as an error bar) of the equivalent diameter (red) and facet length (blue) following electrostatic deposition at two nominal sizes for each of the three polymers (see Table 1).

Evaluating the data points in Figure 3 using eq 3 also leads to the conclusion that the nanoparticles are hollow.

Experimentally we find that SELP nanoparticles possess 4 to 7 facets with the preponderance having 5 or 6, indicating that d_p/L_f should be 2.00 ± 0.30 from the particle geometry considerations in Figure 4b. This ratio can also be determined from 200 nanoparticles captured in TEM images for each of the three polymers at two sizes (25.0 and 39.0 nm for SELP-47K, 29.0 and 38.0 nm for SELP-415K, and 24.0 and 36.0 nm for SELP-815K) with smaller sizes corresponding to peak maxima. Figure 4d shows the compiled means and standard deviations (error bars represent 1σ) for L_f and d_p. Comparing the particle diameter and facet length finds d_p/L_f = 1.95 ± 0.41, which is also in good agreement with theory. Notably the variation in the nanoparticle size remains uniform regardless of diameter in this size range.

Figure 1b also shows several of the nanoparticles to be elongated and rod-shaped (see bottom row). These particles form when the electrospray instability that leads to droplet formation is suppressed.[46] At the exit of the electrospray capillary (see Figure 1a) large electric fields lead to the formation of a Taylor cone, from which a narrow jet emerges. As the jet evolves from the tip of the capillary, a varicose or symmetric perturbation grows on the surface of the jet characterized by a differential radius, L_v, as depicted in Figure 5a. Eggers and Christiani, *et al.*,[47,48] indicate that the jet breaks up into droplets when $2L_v/d_{jet}$ remains less than unity but remains as polymeric filaments when this ratio exceeds unity. The numerator is given by Eggers as $L_v = \mu_l^2/\rho\gamma$,[48] where μ_l, ρ, and γ are the dynamic viscosity, density, and surface tension of the polymer solution. However, d_{jet} is not known *a priori* but must

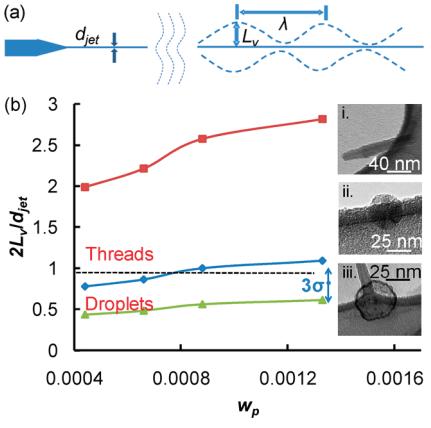

Figure 5. (a) Growth of varicose instability with characteristic period and radius of λ and L_v on an electrospray jet of diameter d_{jet}. (b) Ratio of the characteristic radius of the instability to the diameter of the jet *versus* the polymer concentration for κ = 1.238 S/m (red ■) (C_b = 45 mM and d_{drop} = 100 nm), κ = 0.303 S/m (blue ◆) (C_b = 11 mM and d_{drop} = 200 nm), and κ = 0.028 S/m (green ▲) (C_b = 0.2 mM and d_{drop} = 300 nm). The jet breaks up into droplets for $2L_v/d_{jet} < 1$ and remains as a thread or rod-like structure for $2L_v/d_{jet} > 1$. Mostly spherical and some rod-like structures are formed at w_p = 0.001 33 and C_b = 2 mM, as shown in panels i, ii, and iii, due to variations in d_{jet}.

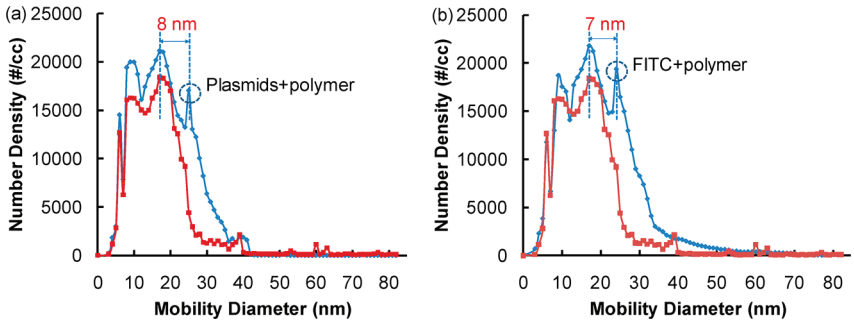

Figure 6. Size distribution of SELP-815K polymer (red ■) at a concentration of w_p = 0.00066 in ammonium acetate buffer at C_b = 2 mM mixed with (a) GFP-labeled DNA plasmids (103 μg/mL) (blue ◆) and (b) fluorescein isothiocyanate (FITC, 1.8 mg/mL) (blue ◆).

be inferred from the model of Christianti, as described in the Methods section. The ratio depends on both the polymer concentration and the conductivity of the electrospray solution, as shown in Figure 5b. Either increases the probability of thread formation.

This comports with our experimental observations. First, increasing the polymer weight fraction to 0.0025 exclusively produces long strands that can be observed visually at the tip of the Taylor cone. Second, depositing all particles emerging from the electrospray at w_p = 0.0013 and C_b = 2 mM finds a minority of particles to be rod-shaped, commensurate with the uncertainty in d_{jet} (see Figure S4 in the Supporting Information). The ability to select for or against rod-like particles is important since it has recently been shown that the shape of nanoparticles can influence biodistribution and cellular uptake.[49,50]

Finally, we demonstrate that these highly uniform nanoparticles may be developed into carriers of therapeutic agents. The advantages of doing so are not only in the precision of the nanoparticle dimensions and tunability of the polymer properties but the ease with which therapeutic agents can be incorporated within these particles. Simply including the therapeutic agent in the polymer solution to be electrosprayed leads to incorporation within the nanoparticle. To demonstrate, we mixed SELP-815K, a polymer shown to maximize duration and extent of gene expression,[19] with plasmid DNA and fluorescein isothiocyanate (FITC) in Figure 6a and b, respectively. In both cases a new peak arises 7−8 nm from the primary peak and the distribution of all particles is wider. The new peaks in the size distributions are remarkably repeatable and strongly indicate the incorporation of these model agents of gene and drug delivery into the SELP nanoparticles (see Figure S5 in the Supporting Information for plasmid size distribution). Further work is underway to analyze their drug release rates and degradation properties both *in vitro* and *in vivo* to prepare the way for their use in gene delivery applications.

MATERIALS AND METHODS

The three SELPs mentioned in Table 1 and collagen-like protein polymer (US patent 5,773,249; Inventors: Joseph Cappello and Franco A. Ferrari) were biosynthesized as described previously.[18] The polymers were stored at −80 °C until diluted in ammonium acetate buffer to the concentrations listed in the figures.

Nanoparticles were fabricated using an electrospray droplet evaporation technique. An ES aerosol generator (TSI 3480) uses pressure-driven flow through a 25 μm capillary. At the tip of the capillary, a voltage was applied to form a Taylor cone. Droplets emitted from the cone were entrained in a mixed stream of air and carbon dioxide at atmospheric pressure.[38] Typical droplets spanned 150 to 300 nm in diameter, though larger sizes were possible.[51,52] Several polymer strands resided within each droplet. As the jet broke up into droplets, they passed through a charge neutralizer (Po-210) to reduce the net charge on the aerosolized droplet to a single net charge.[51,53−55] In the charge neutralizer, as solvent evaporated, the droplet dried and polymeric nanoparticles were formed. Because the droplet size and spatial distribution of strands within the liquid droplet were not necessarily monodisperse and uniform, nanoparticles formed with a distribution of diameters. They entered a differential mobility analyzer (DMA-TSI 3085), where they were purified on the basis of their charge-to-size ratio.[38,52,56−58] Voltage was supplied to the nano-DMA through a high-voltage supply (Bertan 205B-10R).

Within the DMA an aerosolized particle in an electric field, E_s, carrying n_e electric charges experienced an electrostatic force dragging it toward the electrode. The particle very quickly reached its terminal velocity, v, and the electrostatic force acting on the particle was balanced by a resulting drag force on the particle, given by Stokes law, which determines the electrical mobility of a particle,[59] as shown in Figure 1a (see Supporting Information for details). Combining particle and instrument mobilities determines the mobility diameter, d_p, of the particle and is given by

$$\frac{d_p}{C_c} = \frac{2n_e eVL}{3\mu_g q_{sh} \ln \frac{r_2}{r_1}} \quad (4)$$

where the diameter-dependent C_c is the Cunningham slip correction factor,[38] e is the elementary charge on the particle (1.602×10^{-19} C), V is the average voltage on the collector rod inside the DMA, q_{sh} is the sheath flow (nitrogen), μ_g is the gas viscosity, L is the length between polydisperse aerosol inlet and exit slit (4.987 cm), r_1 is the inner radius of annular space of the DMA (0.937 cm), and r_2 is the outer radius of annular space of the DMA (1.905 cm).

Monodispersed aerosol flow exiting the DMA was measured in concentration through an ultrafine condensation particle counter (CPC-TSI 3776) by collecting data for 17 s with a 3 s interval between each measurement or was deposited on a desired substrate (TED PELLA 01824) for TEM imaging using a nanometer aerosol sampler (TSI 3089), which exerts an electric field that collects charged particles from the inlet onto a portion of the substrate.[57] Figure 1a shows a schematic of this setup. The combined electrospray differential mobility analysis system is termed ES-DMA or gas-phase electrophoretic mobility molecular analysis (GEMMA).[51,60]

A transmission electron microscope, FEI Tecnai T-12, was used at high tension (120 kV) to obtain the images of the polymeric nanoparticles. TEM microscopy revealed that these particles have several facets (edges, explained above), and the equivalent diameter was approximated from the TEM images as $d_p = \sum_i L_f^i/\pi$, which is exact for a sphere, where, L_f^i is the length of facet i (see Figure 4a). Histograms were constructed for d_p and average L_f (Figure 2b and Figure 4d) using a midpoint labeled bin.

Sugar solutions in ammonium acetate (2 mM) were used to evaluate the size of the electrospray droplets (see Figure S4 in the Supporting Information). A mass balance between the droplet and the sugar particle yields a relation that the droplet diameter (d_{drop}) is ~19 times the particle diameter (d_p) (see eq S3 in the Supporting Information). A 20 mmol/L ammonium acetate solution (pH ≈ 8) was prepared using milli-Q water, purified by a milli-Q integrated water purification system from Millipore, Inc. Acetic acid and ammonium hydroxide were used to adjust the pH to ~8. Milli-Q water was used for dilution to obtain the reported buffer concentrations. This ensures negligible contribution of nonvolatile salts from the buffer.

The diameter of the jet is a strong function of the viscosity of the solution,[48] and the viscosity of all three polymers under experimental conditions was measured (see Figure S6a in the Supporting Information) using a calibrated semimicroviscometer (Cannon-Manning 9722-D50). A pipet gun was used to apply suction pressure on a glass capillary tube to ensure that humidity did not affect the viscosity measurements. Table 2 gives the values of dynamic viscosity of polymers at different concentrations. Experimental conditions can be found in the Supporting Information. Capillary forces, viscous forces, and electrical stresses govern the growth rate of the perturbation and are characterized by the dimensionless wavenumber, $k' = \pi d_{jet}/\lambda$, which captures the disturbance frequency, the ratio of electrical stress to surface tension, $R_{ES} = \sigma_c^2 d_{jet}/4\gamma\varepsilon_0$, and the Ohnesorge number, $Oh = \mu_l/(\gamma\rho d_{jet})^{1/2}$, which captures the ratio of viscous forces to capillary forces.[46,61,62] Here, d_{jet} is the diameter of the jet, σ_c is the surface charge density, and ε_0 is the permittivity of free space. The perturbation growth rate is a function of d_{jet} and λ (see Figure 5a), calculated using the dispersion relation[46]

$$\omega'^2 + 2^{1/2}Oh\mu_l k'^2\frac{24+k'^2}{8+k'^2}\omega' = \frac{4k'^2}{8+k'^2}\left(1 - k'^2 - 2R_{ES}\left(1 + k'\left(\lim(m \to 0)\frac{I_m'(k') - I'_{-m}(k')}{I_m(k') - I_{-m}(k')}\right)\right)\right) \quad (5)$$

and a mass balance on the jet and droplet,

$$d_{jet} = \left(\frac{2d_{drop}^3}{3\lambda}\right)^{1/2} \quad (6)$$

The jet-breakup phenomenon occurred linearly at the maximum growth rate (see Figure S6b and eq S4 in the Supporting Information), and this jet diameter depended on the droplet diameter. Reasonable initial guesses for d_{jet} and λ yield the maximum growth rate and a corresponding dimensionless wavenumber, k'. k' gives a new characteristic period λ_{new}, and using this value, eq 6 gives a new jet diameter, d_{jet}^{new} for a particular droplet diameter (100−300 nm as in Figure 5b). The maximum growth rate is calculated for this new set of values, and iterations continue until $1 - d_{jet}^{new}/d_{jet}^{old} \leq 10^{-4}$, yielding d_{jet} for different droplet diameters (Figure 5b). When $2L_v/d_{jet} < 1$, the jet breaks up into droplets, and when the ratio is > 1, threads are formed.[62] For our system, the values of the dimensionless numbers are k' = 0.494−1.819, R_{ES} = 0.404−1.85, and Oh = 0.466−1.18.

TABLE 2. Dynamic Viscosities of SELPs at Different Weight Concentrations

polymer	concentration (wt fraction)	viscosity (mPa · s)
SELP-47K	1.33×10^{-3}	1.23
	0.88×10^{-3}	1.19
	0.66×10^{-3}	1.17
	0.44×10^{-3}	1.13
SELP-415K	1.33×10^{-3}	1.30
	0.88×10^{-3}	1.24
	0.66×10^{-3}	1.15
	0.44×10^{-3}	1.09
SELP-815K	1.33×10^{-3}	1.26
	0.88×10^{-3}	1.22
	0.66×10^{-3}	1.18
	0.44×10^{-3}	1.12

Using the ES-DMA fabrication method ~3×10^7 particles can be produced per minute. Industrially, there are several ways to scale-up the throughput. However, the value of the current technique is in separation of the particles not in the way droplets are produced. ES-DMA technique can also be applied to other protein polymers (see Figure S7 in the Supporting Information).

Acknowledgment. L.F.P. recognizes a generous startup package from the University of Utah Chemical Engineering Department and College of Engineering that supported this work. Support was further provided by a grant from the National Institutes of Health (R01CA107621) and an interdisciplinary seed grant from the University of Utah.

Supporting Information Available: An expanded materials and methods section, additional results, and theoretical methods. This material is available free of charge *via* the Internet at http://pubs.acs.org.

REFERENCES AND NOTES

1. Kolbe, A.; Mercato, L. L. D.; Abbas, A. Z.; Gil, P. R.; Gorzini, S. J.; Huibers, W. H. C.; Poolman, B.; Parak, W. J.; Herrmann, A. De Novo Design of Supercharged, Unfolded Protein Polymers, and Their Assembly into Supramolecular Aggregates. *Macromol. Rapid Commun.* **2011**, *32*, 186–190.
2. Yu, A.; Wang, Y.; Barlow, E.; Caruso, F. Mesoporous Silica Particles As Templates for Preparing Enzyme-Loaded Biocompatible Microcapsules. *Adv. Mater.* **2005**, *17*, 1737–1741.
3. Pease, L. F. Optimizing the Yield and Selectivity of High Purity Nanoparticle Clusters. *J. Nanopart. Res.* **2011**, *13*, 2157–2172.
4. Elzey, S.; Grassian, V. H. Agglomeration, Isolation and Dissolution of Commercially Manufactured Silver Nanoparticles in Aqueous Environments. *J. Nanopart. Res.* **2010**, *12*, 1945–1958.
5. Gustafson, J. A.; Ghandehari, H. Silk-Elastinlike Protein Polymers for Matrix-Mediated Cancer Gene Therapy. *Adv. Drug Delivery Rev.* **2010**, *62*, 1509–1523.
6. Cappello, J.; Crissman, J.; Dorman, M.; Mikolajczak, M.; Textor, G.; Marquet, M.; Ferrari, F. Genetic Engineering of Structural Protein Polymers. *Biotechnol. Prog.* **1990**, *6*, 198–202.
7. Megeed, Z.; Cappello, J.; Ghandehari, H. Genetically Engineered Silk-Elastinlike Protein Polymers for Controlled Drug Delivery. *Adv. Drug Delivery Rev.* **2002**, *54*, 1075–1091.
8. Cappello, J.; Crissman, J. W.; Crissman, M.; Ferrari, F. A.; Textor, G.; Wallis, O.; Whitledge, J. R.; Zhou, X.; Burman, D.;

Aukerman, L.; *et al*. In-situ Self-Assembling Protein Polymer Gel Systems for Administration, Delivery, and Release of Drugs. *J. Controlled Release* **1998**, *53*, 105–117.
9. Nagarsekar, A.; Ghandehari, H. Genetically Engineered Polymers for Drug Delivery. *J. Drug Targeting* **1999**, *7*, 11–32.
10. Dinerman, A. A.; Cappello, J.; Ghandehari, H.; Hoag, S. W. Swelling Behavior of a Genetically Engineered Silk-Elastin-like Protein Polymer Hydrogel. *Biomaterials* **2002**, *23*, 4203–4210.
11. Dinerman, A. A.; Cappello, J.; Ghandehari, H.; Hoag, S. W. Solute Diffusion in Genetically Engineered Silk-Elastinlike Protein Polymer Hydrogels. *J. Controlled Release* **2002**, *82*, 277–287.
12. Megeed, Z.; Cappello, J.; Ghandehari, H. Controlled Release of Plasmid DNA from a Genetically Engineered Silk-Elastin-like Hydrogel. *Pharm. Res.* **2002**, *19*, 954–959.
13. Nagarsekar, A.; Crissman, J.; Crissman, M.; Ferrari, F.; Cappello, J.; Ghandehari, H. Genetic Synthesis and Characterization of pH- and Temperature-Sensitive Silk-Elastinlike Protein Block Copolymers. *J. Biomed. Mater. Res.* **2002**, *62*, 195–203.
14. Nagarsekar, A.; Crissman, J.; Crissman, M.; Ferrari, F.; Cappello, J.; Ghandehari, H. Genetic Engineering of Stimuli-Sensitive Silk-Elastinlike Protein Block Copolymers. *Biomacromolecules* **2003**, *4*, 602–607.
15. Megeed, Z.; Haider, M.; Li, D.; O'Malley, B. W., Jr.; Cappello, J.; Ghandehari, H. In Vitro and In Vivo Evaluation of Recombinant Silk-Elastinlike Hydrogels for Cancer Gene Therapy. *J. Controlled Release* **2004**, *94*, 433–445.
16. Haider, M.; Leung, V.; Ferrari, F.; Crissman, J.; Powell, J.; Cappello, J.; Ghandehari, H. Molecular Engineering of Silk-Elastinlike Polymers for Matrix-Mediated Gene Delivery: Biosynthesis and Characterization. *Mol. Pharm.* **2005**, *2*, 139–150.
17. Dandu, R.; Ghandehari, H.; Cappello, J. Characterization of Structurally Related Adenovirus-laden Silk-Elastinlike Hydrogels. *J. Bioact. Compat. Polym.* **2008**, *23*, 5–19.
18. Dandu, R.; Cresce, V. A.; Briber, R.; Dowell, P.; Cappello, J.; Ghandehari, H. Silk-Elastinlike Protein Polymer Hydrogels: Influence of Monomer Sequence on Physicochemical Properties. *Polymer* **2009**, *50*, 366–374.
19. Gustafson, J.; Greish, K.; Frandsen, J.; Cappello, J.; Ghandehari, H. Silk-Elastinlike Recombinant Polymers for Gene Therapy of Head and Neck Cancer: from Molecular Definition to Controlled Gene Expression. *J. Controlled Release* **2009**, *140*, 256–261.
20. Hwang, D.; Moolchandani, V.; Dandu, R.; Haider, M.; Cappello, J.; Ghandehari, H. Influence of Polymer Structure and Biodegradation on DNA Release from Silk-Elastinlike Protein Polymer Hydrogels. *Int. J. Pharm.* **2009**, *368*, 215–219.
21. Hogan, C. J., Jr.; Yun, K. M.; Chen, D. R.; Lenggoro, I. W.; Biswas, P.; Okuyama, K. Controlled Size Polymer Particle Production via Electrohydrodynamic Atomization. *Colloids Surf., A* **2007**, *311*, 67–76.
22. Hung, L. H.; Lee, A. P. Microfluidic Devices for the Synthesis of Nanoparticles and Biomaterials. *J. Med. Biol. Eng.* **2007**, *27*, 1–6.
23. Widiyandari, H.; Hogan, C. J., Jr.; Yun, K. M.; Iskandar, F.; Biswas, P.; Okuyama, K. Production of Narrow-Size-Distribution Polymer-Pigment-Nanoparticle Composites via Electrohydrodynamic Atomization. *Macromol. Mater. Eng.* **2007**, *292*, 495–502.
24. Yang, S. Y.; Cheng, F. Y.; Yeh, C. S.; Lee, G. B. Size-Controlled Synthesis of Gold Nanoparticles Using a Micro-Mixing System. *Microfluid Nanofluid* **2010**, *8*, 303–311.
25. Nie, Z.; Xu, S.; Seo, M.; Lewis, P. C.; Kumacheva, E. Polymer Particles with Various Shapes and Morphologies Produced in Continuous Microfluidic Reactors. *J. Am. Chem. Soc.* **2005**, *127*, 8058–8063.
26. Johnson, B. K.; Prud'homme, R. K. Mechanism for Rapid Self-Assembly of Block Copolymer Nanoparticles. *Phys. Rev. Lett.* **2003**, *91*, 118302-1–118302-4.
27. Johnson, B. K.; Prud'homme, R. K. Chemical Processing and Micromixing in Confined Impinging Jets. *AIChE J.* **2003**, *49*, 2264–2282.
28. Johnson, B. K.; Prud'homme, R. K. Flash Nanoprecipitation of Organic Actives and Block Copolymers Using a Confined Impinging Jets Mixer. *Aust. J. Chem.* **2003**, *56*, 1021–1024.
29. Zhu, Z.; Anacker, J. L.; Ji, S.; Hoye, T. R.; Macosko, C. W.; Prud'homme, R. K. Formation of Block Copolymer-Protected Nanoparticles via Reactive Impingement Mixing. *Langmuir* **2007**, *23*, 10499–10504.
30. Wu, Y.; MacKay, J. A.; McDaniel, J. R.; Chilkoti, A.; Clark, R. L. Fabrication of Elastin-Like Polypeptide Nanoparticles for Drug Delivery by Electrospraying. *Biomacromolecules* **2009**, *10*, 19–24.
31. Valo, H.; Peltonen, L.; Vehvilainen, S.; Karjalainen, M.; Kostiainen, R.; Laaksonen, T.; Hirvonen, J. Electrospray Encapsulation of Hydrophilic and Hydrophobic Drugs in Poly(L-lactic acid) Nanoparticles. *Small* **2009**, *5*, 1791–1798.
32. Dash, B. C.; Mahor, S.; Carroll, O.; Mathew, A.; Wang, W.; Woodhouse, K. A.; Pandit, A. Tunable Elastin-Like Polypeptide Hollow Sphere As a High Payload and Controlled Delivery Gene Depot. *J. Controlled Release 152*, 382−392.
33. Rethore, G.; Mathew, A.; Naik, H.; Pandit, A. Preparation of Chitosan/Polyglutamic Acid Spheres Based on the Use of Polystyrene Template As a Nonviral Gene Carrier. *Tissue Eng. Part C: Methods* **2009**, *15*, 605–613.
34. Tsai, D. H.; Zangmeister, R. A.; Pease, L. F.; Tarlov, M. J.; Zachariah, M. R. Gas-Phase Ion-Mobility Characterization of SAM-Functionalized Au Nanoparticles. *Langmuir* **2008**, *24*, 8483–8490.
35. Greish, K.; Frandsen, J.; Scharff, S.; Gustafson, J.; Cappello, J.; Li, D.; O'Malley, B. W., Jr.; Ghandehari, H. Silk-Elastinlike Protein Polymers Improve the Efficacy of Adenovirus Thymidine Kinase Enzyme Prodrug Therapy of Head and Neck Tumors. *J. Gene Med.* **2010**, *12*, 572–579.
36. Stolzenburg, M. R. An Ultrafine Aerosol Size Distribution Measuring System. Ph.D Thesis. University of Minnesota, Minneapolis, 1988.
37. Stolzenburg, M. R.; McMurry, P. H. Equations Governing Single and Tandem DMA Configurations and a New Lognormal Approximation to the Transfer Function. *Aerosol Sci. Technol.* **2008**, *42*, 421–432.
38. Pease, L. F.; Tsai, D. H.; Zangmeister, R. A.; Zachariah, M. R.; Tarlov, M. J. Quantifying the Surface Coverage of Conjugate Molecules on Functionalized Nanoparticles. *J. Phys. Chem. C* **2007**, *111*, 17155–17157.
39. Cole, K. D.; Pease, L. F.; Tsai, D. H.; Singh, T.; Lute, S.; Brorson, K. A.; Wang, L. Particle Concentration Measurement of Virus Samples Using Electrospray Differential Mobility Analysis and Quantitative Amino Acid Analysis. *J. Chromatogr. A* **2009**, *1216*, 5715–5722.
40. Lute, S.; Riordan, W.; Pease, L. F.; Tsai, D. H.; Levy, R.; Haque, M.; Martin, J.; Moroe, I.; Sato, T.; Morgan, M.; *et al*. A Consensus Rating Method for Small Virus-Retentive Filters. I. Method Development. *PDA J. Pharm. Sci. Technol.* **2008**, *62*, 318–333.
41. Fernandez de la Mora, J.; Loscertales, I. G. The Current Emitted by Highly Conducting Tayloer Cones. *J. Fluid. Mech.* **1994**, *260*, 155–184.
42. Pauchard, L.; Allain, C. Buckling Instability Induced by Polymer Solution Drying. *Europhys. Lett.* **2003**, *62*, 897–903.
43. Parisse, F.; Allain, C. Drying of Collodial Suspension Droplets: Experimental Study and Profile Renormalization. *Langmuir* **1997**, *13*, 3598–3602.
44. Fischer, B. J. Particle Convection in an Evaporating Colloidal Droplet. *Langmuir* **2002**, *18*, 60–67.
45. Landau, L. D.; Lifshitz, E. M. *Theory of Elasticity*; Pergamon Press, 1959; Vol. 7, pp 62−65.
46. Hartman, R. P. A.; Brunner, D. J.; Camelot, D. M. A.; Marijnissen, J. C. M.; Scarlett, B. Jet Break-up in Electrohydrodynamic Atomization in the Cone-Jet Mode. *J. Aerosol Sci.* **2000**, *31*, 65–95.
47. Christanti, Y.; Walker, L. M. Surface Tension Driven Jet Breakup of Strain-Hardening Polymer Solutions. *J. Non-Newtonian Fluid Mech.* **2001**, *100*, 9–26.
48. Eggers, J. Universal Pinching of 3D Axisymmetric Free-Surface Flow. *Phys. Rev. Lett.* **1993**, *71*, 3458–3460.

49. Gratton, S. E.; Ropp, P. A.; Pohlhaus, P. D.; Luft, J. C.; Madden, V. J.; Napier, M. E.; DeSimone, J. M. The Effect of Particle Design on Cellular Internalization Pathways. *Proc. Natl. Acad. Sci. U. S. A.* **2008**, *105*, 11613–11618.
50. Arnida; Janat-Amsbury, M. M.; Ray, A.; Peterson, C. M.; Ghandehari, H. Geometry and Surface Characteristics of Gold Nanoparticles Influence their Biodistribution and Uptake by Macrophages. *Eur. J. Pharm. Biopharm.* **2011**, *12*, 88-96. doi:10.1016/j.ejpb.2010.11.010.
51. Bacher, G.; Szymanski, W. W.; Kaufman, S. L.; Zollner, P.; Blaas, D.; Allmaier, G. Charge-Reduced Nano Electrospray Ionization Combined with Differential Mobility Analysis of Peptides, Proteins, Glycoproteins, Noncovalent Protein Complexes and Viruses. *J. Mass Spectrom.* **2001**, *36*, 1038–1052.
52. Pease, L. F.; Elliott, J. T.; Tsai, D. H.; Zachariah, M. R.; Tarlov, M. J. Determination of Protein Aggregation with Differential Mobility Analysis: Application to IgG Antibody. *Biotechnol. Bioeng.* **2008**, *101*, 1214–1222.
53. Smith, J. N.; Flagan, R. C.; Beauchamp, J. L. Droplet Evaporation and Discharge Dynamics in Electrospray Ionization. *J. Phys. Chem. A* **2002**, *106*, 9957–9967.
54. Chen, D. R.; Pui, D. Y. H.; Kaufman, S. L. Electrospraying of Conducting Liquids for Monodisperse Aerosol Generation in the 4 nm to 1.8 μm Diameter Range. *J. Aerosol Sci.* **1995**, *26*, 963–977.
55. Wiedensohler, A.; Lütkemeier, E.; Feldpausch, M.; Helsper, C. Investigation of the Bipolar Charge Distribution at Various Gas Conditions. *J. Aerosol Sci.* **1986**, *17*, 413–416.
56. Pease, L. F.; Tsai, D. H.; Fagan, J. A.; Bauer, B. J.; Zangmeister, R. A.; Tarlov, M. J.; Zachariah, M. R. Length Distribution of Single-Walled Carbon Nanotubes in Aqueous Suspension Measured by Electrospray Differential Mobility Analysis. *Small* **2009**, *5*, 2894–2901.
57. Fuchs, N. A. On the Stationary Charge Distribution on Aerosol Particles in a Bipolar Ionic Atmosphere. *Pure Appl. Geophys.* **1963**, *56*, 185–193.
58. Wiedensohler, A.; Fissan, H. J. An Approximation of the Bipolar Charge Distribution for Particles in the Submicron Size Range. *J. Aerosol Sci.* **1988**, *19*, 387–389.
59. Knutson, E. O.; Whitby, K. T. Aerosol Classification by Electric Mobility: Apparatus, Theory, and Applications. *J. Aerosol Sci.* **1975**, *6*, 443–451.
60. Saucy, D. A.; Ude, S.; Lenggoro, I. W.; Fernandez de la Mora, J. Mass Analysis of Water-Soluble Polymers by Mobility Measurement of Charge-Reduced Ions Generated by Electrosprays. *Anal. Chem.* **2004**, *76*, 1045–1053.
61. Christanti, Y.; Walker, L. M. Effect of Fluid Relaxation Time of Dilute Polymer Solutions on Jet Breakup Due to a Forced Disturbance. *J. Rheol.* **2002**, *46*, 733–748.
62. Christanti, Y.; Walker, L. M. Surface Tension Driven Jet Breakup of Strain-Hardening Polymer Solutions. *J. Non-Newtonian Fluid Mech.* **2001**, *100*, 9–26.